Proceedings of the ASME 2012 International Mechanical Engineering Congress & Exposition
November 9-15, 2012, Houston, Texas

IMECE2012-87713

EXTENDED FINITE ELEMENT ANALYSIS OF JOURNAL BEARING DYNAMIC FORCED PERFORMANCE TO INCLUDE FLUID INERTIA FORCE COEFFICIENTS

Luis San Andrés
Fellow ASME
lsanandres@tamu.edu
Turbomachinery Laboratory
Texas A&M University
College Station, TX 77843

ABSTRACT

Reynolds equation governs the generation of hydrodynamic pressure in oil lubricated fluid film bearings. The static and dynamic forced response of a bearing is obtained from integration of the film pressure on the bearing surface. For small amplitude journal motions, a linear analysis represents the fluid film bearing reaction forces as proportional to the journal center displacements and velocity components through four stiffness and four damping coefficients. These force coefficients are integrated into rotor-bearing system structural analysis for prediction of the system stability and the synchronous response to imbalance. Fluid inertia force coefficients, those relating reaction forces to journal center accelerations, are routinely ignored because most oil lubricated bearings operate at relatively low Reynolds numbers, i.e., under slow flow conditions. Modern rotating machinery operates at ever increasing surface speeds to deliver more power in smaller size units. Under these operating conditions fluid inertia effects need to be accounted for in the forced response of oil lubricated bearings, as recent experimental test data also reveal. The paper presents a finite element formulation to predict added mass coefficients in oil lubricated bearings by extending a basic formulation that already calculates the bearing stiffness and damping force coefficients. That is, a small amplitude perturbation analysis of the lubrication flow equations keeps the temporal fluid inertia effects and develops a set of equations to obtain the bearing stiffness, damping and inertia force coefficients. The method does not impose on the cost of the original formulation which makes it very attractive for ready implementation in existing software. Predictions of the computational model are benchmarked against archival test data for an oil-lubricated pressure dam bearing supporting large compressors. The comparisons show fluid inertia effects cannot be ignored for operation at high rotor speeds and with small static loads.

INTRODUCTION

Analysis of the dynamic performance of rotors supported on fluid film bearings relies not just on the rotor structural (mass and elastic) properties but also on the acurate evaluation of the static and dynamic forced performance characteristics of the bearing supports. A rotordynamic analysis delivers synchronous response to imbalance and system stability results in accordance with API requirements, to demonstrate certain performance characteristics; and on occasion, to reproduce peculiar field phenomena and to troubleshoot malfunctions or limitations of the operating system.

Mineral-oil lubricated bearings support most commercial machinery that operate at low to moderately high rotational shaft speeds. The bearings carry heavy static loads, mainly a fraction of the rotor weight. The lubricant, supplied from an external reservoir, fills the small clearance separating the shaft (journal) from the bearing. Shaft rotation drags the lubricant through the bearing film lands to form the hydrodynamic wedge that generates the hydrodynamic fluid film pressure that, acting on the journal, is able to support or carry the applied static load. The mineral oil lubricant, generally of large viscosity, increases its temperature as it carries away the mechanical energy dissipated into heat. Hence, the material visosity of the lubricant, a strong function of temperature, does not remain constant within the film flow region in the bearing.

Importantly enough, the conditions of low speed (Ω), small clarance *(c)*, and large viscosity (μ/ρ) determine a laminar flow condition in the bearing, i.e. operation with small Reynolds numbers Re < 1,000 ($\mathrm{Re}=\rho\Omega Rc/\mu$). Hence, Reynolds equation of Classical Lubrication is valid for prediction of the equilibrium hydrodynamic film pressure in the bearing. The prediction of the thermal energy transport in a thin film bearing is more difficult since there is a significant temperature along and accross the film, i.e. a three-dimensional phenomenon. Most importantly, the thermal energy exchange does not just involve the mechanical energy generated by shear and its advection by the lubricant flow but also must account for the heat conduction into or from the shaft and bearing cartridge.

A comprehensive 3-D thermohydrodynamic analysis for prediction of performance in finite length journal bearings is out of the scope of the current analysis. The interested reader should refer to relevant work in the archival literature [1,2] for

 Copyright © 2012 by ASME

further details. However, note that most fluid film bearing designers and bearing manufacturers rarely rely on cumbersome and computationally expensive analysis tools; in particular when they require of boundary conditions that are operating system dependent (not general). More than often, engineers prefer to obtain model results that are in agreement with published test data and go along with their vast practical experience.

ANALYSIS

Figure 1 depicts the geometry of typical pad in a bearing and a journal rotating with angular speed (Ω). A film of lubricant fills the gap between the bearing and its journal. Journal center dislacements (e_X, e_Y) refer to the (X,Y) inertial coordinate system. The angle Θ, whose origin is at the $-X$ axis, aids to describe the film geometry. The graphs show the relevant nomenclature for analysis

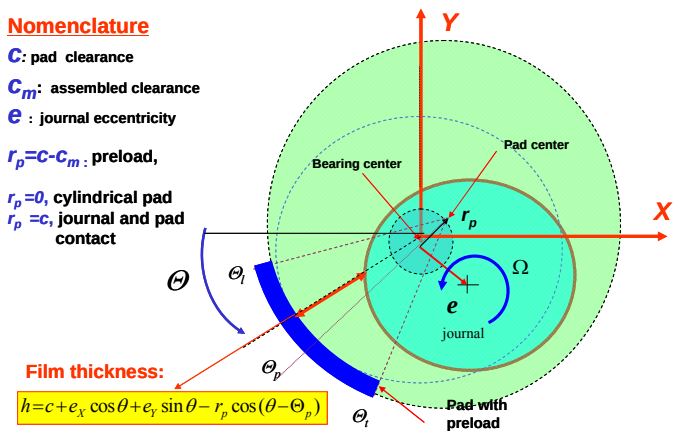

Fig. 1. Geometry of a bearing pad with preload and description of film thickness (not to scale).

Within the flow region $\{\Theta_l \le \Theta \le \Theta_t,\ 0 < z < L\}$, the film thickness *(h)* is

$$h = c - r_p \cos(\Theta - \Theta_p) + e_{X(t)} \cos\Theta + e_{Y(t)} \sin\Theta \qquad (1)$$

where r_p is the pad preload at the offset angle Θ_P. The modified laminar flow Reynolds equation describing the generation of hydrodynamic pressure (P) in the thin film region of a bearing pad is [3,4,5]

$$\frac{1}{R^2}\frac{\partial}{\partial\Theta}\left(\frac{h^3}{12\mu_{(T)}}\frac{\partial P}{\partial\Theta}\right)+\frac{\partial}{\partial z}\left(\frac{h^3}{12\mu_{(T)}}\frac{\partial P}{\partial z}\right)= \frac{\partial h}{\partial t}+\frac{\Omega}{2}\frac{\partial h}{\partial\Theta}+\left(\frac{\rho h^2}{12\mu_{(T)}}\right)\frac{\partial^2 h}{\partial t^2} \qquad (2)$$

where (ρ, μ) denote the lubricant density and viscosity, both temperature (T) dependent material properties. The modified Reynolds equation includes temporal fluid inertia effects; hence, the flow model is strictly applicable to lubricant thin film flows induced by small amplitude journal motions about an equilibrium position [5]. Presently, the lubricant visosity is assumed constant and hence thermal effects are altogether neglected. Please see Ref. [6], for a more detailed analysis implementing a bulk-flow temperature for the thermal energy transport in the fluid film region.

Boundary conditions At a pad leading edge the presure equals a supply condition, i.e.

$$0 \le z \le L : P(\Theta_l, z) = P_S \qquad (3a)$$

The pressure is ambient at the bearing axial ends,

$$\Theta_l \le \Theta \le \Theta_t : P(\Theta,0) = P_a\ ;\quad P(\Theta,L) = P_a\ ; \qquad (3b)$$

and also at the pad trailing edge,

$$0 \le z \le L : P(\Theta_t, z) = P_a \qquad (3c)$$

Furthermore, within the whole flow domain, $P > P_{cav}$, i.e., the film pressure must be higher than the lubricant cavitation pressure. Read Ref. [7] for a thorough discussion on lubricant cavitation and the formulation of physical sound boundary conditions.

Consider small amplitude journal motions (Δe_X, Δe_Y) with whirl frequency ω about the equilibrium position (e_{X_0}, e_{Y_0}), as shown in Fig. 2. The film thickness *(h)* is the real part of

$$h = h_0 + [\Delta e_X \cos\Theta + \Delta e_Y \sin\Theta]\, e^{i\omega t} = = h_0 + \Delta e_\sigma h_\sigma e^{i\omega t}\ ;\ {}_{\sigma=X,Y};\ \ i = \sqrt{-1} \qquad (4)$$

with h_0 as the equilibrium film thickness and $h_X = \cos\Theta$, $h_Y = \sin\Theta$.

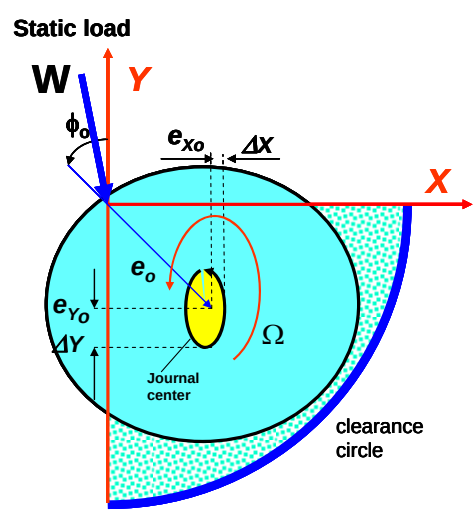

Fig. 2 Depiction of small amplitude journal motions about an equilibrium position (Not to scale).

The pressure field is also the superposition of zeroth and first order fields:

$$P = P_0 + \Delta e_\sigma P_\sigma e^{i\omega t}\ ;\ {}_{\sigma=X,Y}\,. \qquad (5)$$

Copyright © 2012 by ASME

The zeroth-order (P_0) is the equilibrium pressure field governed by

$$L(P_0) = \frac{1}{R^2}\frac{\partial}{\partial\Theta}\left(\frac{h_0^3}{12\mu}\frac{\partial P_0}{\partial\Theta}\right) + \frac{\partial}{\partial z}\left(\frac{h_0^3}{12\mu}\frac{\partial P_0}{\partial z}\right) = \frac{\Omega R}{2}\frac{\partial h_0}{R\,\partial\Theta} \tag{6}$$

and the first-order complex pressure fields $P_{\sigma=X,Y}$ due to the journal center dynamic displacements satisfy

$$L(P_\sigma) = \frac{\partial}{R\,\partial\Theta}\left(\frac{\Omega R}{2}h_\sigma - \frac{3h_0^2}{12\mu}h_\sigma\frac{\partial P_0}{R\,\partial\Theta}\right) - \frac{\partial}{\partial z}\left(\frac{3h_0^2 h_\sigma}{12\mu}\frac{\partial P_0}{\partial z}\right) + \left\{\boldsymbol{i} - \left(\frac{\rho h_0^2\omega}{12\mu}\right)\right\}\omega h_\sigma \tag{7}$$

with σ=X,Y. Above $\mathrm{Re}_s = \rho h_0^2\omega / \mu$ is a (modified) squeeze film Reynolds number. Eqs. (3) already states the boundary conditions for the zeroth order pressure. The first-order pressure fields $P_{\sigma=X,Y}$ =0 on the boundary of a bearing pad.

Once the pressure fields are determined, the components of the fluid film bearing reaction force **F** are

$$F_\sigma = \sum_{k=1}^{N_{pad}}\int_0^L\int_{\Theta_k}\left\{P_0 + \Delta e_\sigma P_\sigma e^{i\omega t}\right\}_k h_\sigma\, R\, d\Theta_k\, dz = F_{\sigma_0} - Z_{\sigma\beta}\,\Delta e_\sigma\, e^{i\omega t}\ ;\quad \sigma,\beta=X,Y \tag{8}$$

where $\mathbf{F_o}$+**W=0** represents the balance of static forces. The bearing impedances ($Z_{\beta\sigma}$), delivering the stiffness, damping and inertia force coefficients $(K, C, M)_{\alpha\beta=X,Y}$, are evaluated from the real and imaginary parts of

$$Z_{\beta\sigma} = \left(K_{\beta\sigma} - \omega^2 M_{\beta\sigma}\right) + \boldsymbol{i}\,\omega C_{\beta\sigma} = -\sum_{k=1}^{N_{pad}}\int_0^L\int_{\Theta_k} P_{\sigma_k}\, h_\beta\, R\, d\Theta_k\, dz\ ;\qquad \beta,\sigma=X,Y \tag{9}$$

The numerical solution method

The finite element method (FEM) is well suited for the numerical solution of elliptic type differential equations such as the Reynolds Equation. Complicated geometrical domains are well represented by finite elements, thus its major advantage over other methods such as finite differences. Another major advantage will be shown later as the systems of equations for solution of the zeroth and first order pressure fields have the same (global) fluidity matrix. This feature allows the most rapid evaluation of the bearing linearized force coefficients.

Fig. 3 depicts a flow region divided into a collection of N_{em} four-noded isoparametric finite elements. The pressure over an element (Ω^e) is given by a linear combination of nodal values $\left\{\overline{P}_i\right\}_{=1}^{n_{pe}}$ and bilinear shape functions $\left\{\Psi_i^e\right\}_{=1}^{n_{pe}}$, i.e.,

$$P_0^e = \sum_{i=1}^{n_{pe}}\Psi_i^e\overline{P}_{0_i}^e\ ,\quad P_\sigma^e = \sum_{i=1}^{n_{pe}}\Psi_i^e\overline{P}_{\sigma_i}^e\ ;\quad \sigma=X,Y \tag{10}$$

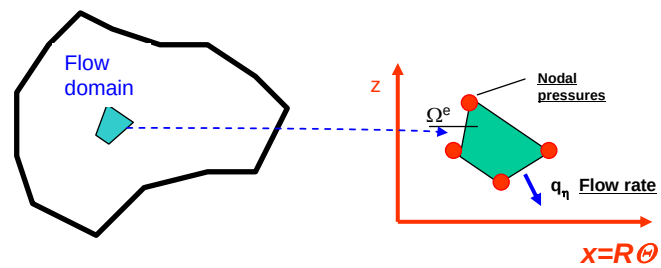

Fig 3. Depiction of general domain of flow field and finite element representation.

Within element (Ω^e), the Galerkin formulation [10] transforms Eq. (6) for the equilibrium field P_0 into the algebraic system of linear equations

$$\mathbf{k^e}\,\overline{\mathbf{P}}_0^{\mathbf{e}} = -\mathbf{q}_0^{\mathbf{e}} + \mathbf{f}_0^{\mathbf{e}}\ : \tag{11}$$

where the coefficients of the element fluidity matrix ($\mathbf{k^e}$) are

$$k_{ij}^e = k_{ji}^e = \iint_{\Omega^e}\left(\frac{h_0^3}{12\mu}\right)^e\left\{\Psi_{i,x}\Psi_{j,x} + \Psi_{i,z}\Psi_{j,z}\right\}^e dx\, dz \qquad i,j=1,..N_{pe} \tag{12a}$$

with $\Psi_{i,x} = \partial\Psi_i / \partial x$ and $\Psi_{i,z} = \partial\Psi_i / \partial z$. In Eq. (11), the vectors $\mathbf{f_0}$ and $\mathbf{q_0}$ denote shear flow effects and the nodal flow rates:

$$f_{0_i}^e = \frac{\Omega R}{2}\iint_{\Omega^e}\left(h_0\frac{\partial\Psi_i}{\partial x}\right)^e dx\, dz\ ;\qquad q_{0_i}^e = \oint_{\Gamma^e}\Psi_i^e q_{\eta_0}\, d\Gamma^e \tag{12b}$$

with

$$q_{\eta_0} = -\frac{h_0^3}{12\mu}\frac{\partial P_0}{\partial\eta} + \frac{h_0\,\Omega R}{2}\eta_x \tag{13}$$

as the flow through the element boundary (Γ^e).

The integrals in Eqns. (12) are evaluated numerically over a master isoparametric element ($\hat{\Omega}$) with normalized coordinates. Reddy and Gartling [11] explain the coordinate transformation and numerical integration procedure using Gauss-Legendre quadrature formulas.

Eqns. (11) are assembled over the whole flow domain and then condensed by enforcing the corresponding boundary conditions. The resultant global set of equations is

$$\mathbf{k_G}\,\overline{\mathbf{P}}_{\mathbf{G_0}} = -\mathbf{Q_G} + \mathbf{F_G} \tag{14}$$

where $\mathbf{k_G} = \bigcup_{e=1}^{Nem}\mathbf{k^e}$, $\mathbf{Q_G} = \bigcup_{e=1}^{Nem}\mathbf{q^e}$, $\mathbf{F_G} = \bigcup_{e=1}^{Nem}\mathbf{f^e}$. The global fluidity matrix $\mathbf{k_G}$ is symmetric, easily decomposed into its upper and lower triangular form (Cholesky algorithm), i.e.,

$$\mathbf{K_G} = \mathbf{L_G}\,\mathbf{L_G^T} \tag{15}$$

A process of back- and forward-substitutions then renders the discrete zeroth order pressure field $\overline{\mathbf{P}}_{\mathbf{G_0}}$

$$\mathbf{L_G}\left(\mathbf{L_G^T}\,\overline{\mathbf{P}}_{\mathbf{G_0}}\right) = -\mathbf{Q_G} + \mathbf{F_G} \tag{16}$$

Copyright © 2012 by ASME

Note that $\mathbf{Q_G=0}$ denotes the addition of flow rates at a node. Hence the components of this vector are zero at each internal node of the flow domain.

A similar procedure follows for solution of the perturbed (dynamic) pressure fields, P_X and P_Y, due to journal harmonic displacements (Δe_X, Δe_Y) with whirl frequency ω. The weak or variational form of Eqns. (7) become

$$\mathbf{k^e}\,\overline{\mathbf{P}}^{\mathbf{e}}_{\sigma} = \mathbf{f}^{\mathbf{e}}_{\sigma} - \mathbf{S}^{\mathbf{e}}_{\sigma}\overline{\mathbf{P}}^{\mathbf{e}}_{0} - \mathbf{q}^{\mathbf{e}}_{\sigma} \tag{17}$$

i,j=1,..N_{pe} and σ=X,Y. Above,

$$f_{\sigma_i}^{\ e} = \frac{\Omega R}{2}\iint_{\Omega^e} h_\sigma \Psi^e_{i,x}\,dxdz + \omega^2 \iint_{\Omega^e} h_\sigma \left[\frac{\rho h_0^2}{12\mu}\right]^e \Psi^e_i\,dxdz - \boldsymbol{i}\,\omega \iint_{\Omega^e} h_\sigma \Psi^e_i\,dxdz \tag{18a}$$

$$S_{\sigma_{ij}}^{\ e} = \iint_{\Omega^e}\left(\frac{3h_0^2\,h_\sigma}{12\mu_{(T)}}\right)^e \left\{\Psi_{i,x}\Psi_{j,x} + \Psi_{i,z}\Psi_{j,z}\right\}^e dx\,dz \tag{18b}$$

and

$$q_{\sigma i}^{\ e} = \oint_{\Gamma^e} \Psi^e_i\, q_{\eta_\sigma}\, d\Gamma^e \tag{18c}$$

with $$q_{\eta_\sigma} = -\frac{h_0^3}{12\mu}\frac{\partial P_\sigma}{\partial \eta} - \frac{3h_0^2\,h_\sigma}{12\mu}\frac{\partial P_0}{\partial \eta} + \frac{\Omega R}{2} h_\sigma\,\eta_x \tag{18d}$$

as the first-order (perturbed) flow rates.

Note that the FE formulation detailed conserves the fluid flow across elements of different film thicknesses, such as in steps, pockets and grooves [12].

Eqns. (17) are assembled over the whole flow domain and then condensed by enforcing the homogenous boundary conditions. The resultant global set of equations for perturbations along the X and Y axes are:

$$\mathbf{K_G}\,\overline{\mathbf{P}}_{\mathbf{G_X}} = -\mathbf{Q}_{\mathbf{G_X}} + \mathbf{F}_{\mathbf{G_X}} - \mathbf{S}_{\mathbf{G_X}}\overline{\mathbf{P}}_{\mathbf{G_0}}$$
$$\mathbf{K_G}\,\overline{\mathbf{P}}_{\mathbf{G_Y}} = -\mathbf{Q}_{\mathbf{G_Y}} + \mathbf{F}_{\mathbf{G_Y}} - \mathbf{S}_{\mathbf{G_Y}}\overline{\mathbf{P}}_{\mathbf{G_0}} \tag{19}$$

Thus, the assembly process of the first order equations renders a fluidity matrix ($\mathbf{K_G}$) identical to that for the equilibrium pressure field. The perturbed pressure fields can be calculated rapidly since $\mathbf{K_G}$ was originally obtained and decomposed in the procedure to find the equilibrium pressure field, see Eq. (15).

To solve Eqs. (15) and (19) the backward and forward substitution procedures, avoiding matrix inversion, are written as

$$\text{given}\left(\mathbf{L_G}\,\mathbf{L_G^T}\right)\mathbf{P_G} = \mathbf{R_G}\text{, solve}$$
$$\mathbf{L_G}\,\mathbf{Z_G} = \mathbf{R_G} \rightarrow \text{find } \mathbf{Z_G} \text{ by backward substitutions} \tag{20}$$
$$\mathbf{L_G^T}\,\mathbf{P_G} = \mathbf{Z_G} \rightarrow \text{find } \mathbf{P_G} \text{ by forward substitutions}$$

In practice, the numerical process does not require specification of a whirl frequency (ω) nor conducting several calculations to discern the stiffnesses from the mass coefficients [6]. That is, the right hand side vector in Eq. (17) can be can be decomposed into its real and imaginary parts,

$$\mathbf{f}^{\mathbf{e}}_{\sigma} - \mathbf{S}^{\mathbf{e}}_{\sigma}\overline{\mathbf{P}}^{\mathbf{e}}_{0} = \left({}^{R}\mathbf{f}^{\mathbf{e}}_{\sigma_K} - \mathbf{S}^{\mathbf{e}}_{\sigma}\overline{\mathbf{P}}^{\mathbf{e}}_{0}\right) + \omega^2\,{}^{R}\mathbf{f}^{\mathbf{e}}_{\sigma_M} + \boldsymbol{i}\,\omega\,{}^{I}\mathbf{f}^{\mathbf{e}}_{\sigma} \tag{21}$$

The imaginary part will lead to the evaluation of the first-order pressure from which to determine the damping coefficients $\left(C_{\beta\sigma}\right)_{\beta,\sigma=X,Y}$. The real part has two components, one that will give the perturbed pressures determining the stiffness coefficients $\left(K_{\beta\sigma}\right)_{\beta,\sigma=X,Y}$; and the second part, proportional to ω^2, will give the pressures rendering the fluid inertia coefficients $\left(M_{\beta\sigma}\right)_{\beta,\sigma=X,Y}$.

Thus, a FE computational program that already calculates bearing stiffness and damping force coefficients can be readily extended, with minimum effort and expedience in computations, to evaluate inertia force coefficients.

PREDICTIONS AND COMPARISONS TO TEST DATA

Model predictions for test bearings reported in the literature were obtained. The benchmark cases included one . grooved bearing and [13] and a two grooved journal bearing [14]. In general, the predictions for static load performance conditions are in good agreement with the test data. In addition, for ideal cylindrical journal bearing configurations $\left(L/D \rightarrow 0, L/D \rightarrow \infty\right)$, the computational model reproduces force coefficients, including fluid inertia, identical to those reported in the archival literature [3,4,5].

Presently, model predictions for the static and dynamic load performance of a pressure dam journal bearing are compared against exhaustive test data acquired by Jughaiman and Childs [15]. Figure 4 shows a schematic view of the tests bearing and Table 1 lists the bearing geometry and operating condition. Ref. [15] misses details on the bearing geometry, lubricant inlet and feed conditions. Note that the pressure dam depth to clearance ratio and dam arc length relative to pad arc length follow standard best practices recommended by Nicholas and Allaire [16].

In the experiments, ISO VG 32 lubricant fills the thin film lands of the pressure dam bearing. An air turbine drives the test rigid shaft supported on ball bearings. The test bearing *floats* on the rotating shaft. The tester includes a hydraulic cylinder for static loading, and stinger connections to hydraulic shakers that excite the floating test bearing. The instrumentation includes load cells attached to the shaker stingers, eddy current sensors mounted on the bearing and facing the shaft, and accelerometers attached to the bearing housing. The parameter identification method is based on frequency domain measurements and extracts the force coefficients from curve fits of the real and imaginary parts of the test system impedances.

The maximum load (W) applied equals 12 kN (2,700 lb_f) which gives a specific pressure (W/LD) = 1.345 MPa (~ 200 psi). It is important to note that for the nominal clearance of 0.142 mm and operation at 10 krpm (Ω=1048 rad/s), the shear

Copyright © 2012 by ASME

flow Reynolds number ($\rho\Omega Rc/\mu$) = 321, thus denoting laminar flow conditions. The squeeze film Reynolds number $Re_s=(\rho\Omega c^2/\mu)$ is just 0.8, which could mislead one to ignore fluid fluid inertia effects.

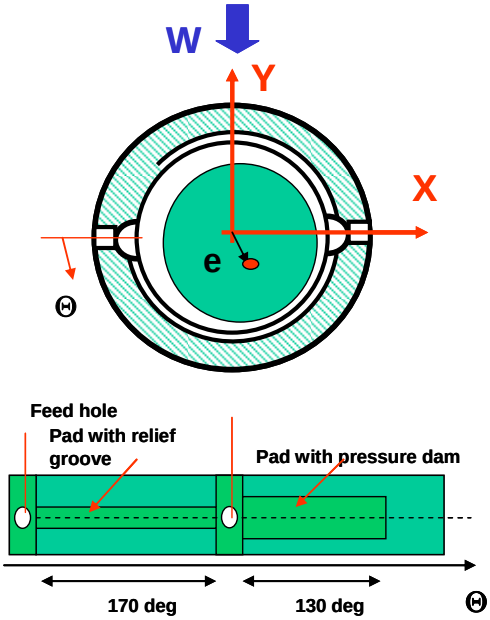

Fig. 4 Schematic view of pressure dam bearing with a relief groove.

Table 1. Dimensions and operating conditions of pressure dam bearing tested by Al-Jughaiman and Childs [15]

Journal diameter	D	117.1	mm
Bearing Length	L	76.2	mm
Radial clearance	c	0.142	mm
pad arc		170°	
Dam arc length	Θ_D	130	deg
width (0.75 L)	L_D	57.1	mm
depth		0.4	mm
Relief groove width	L_R	19.05	mm
depth		0.1	mm
Lubricant	**ISO VG 32**		
Density	ρ	860	kg/m^3
Specific Heat	Cp	2,000	J/kg-°C
Thermal conductivity	k	0.13	W/m-°C
Viscosity at 45 C	μ	0.028	Pa.s
Visc.-temp coefficient	α	0.034	1/°C
Inlet oil temperature		40-55	°C
Inlet oil pressure		N/A	MPa
Applied load range:	0.1-12.0	kN	
Journal speed range:	4, 6, 8, 10, 12	krpm	

In the following figures, lines denote predictions from the current model and symbols represent the measurements. Note that Ref. [15] does not always report parameters for all the listed test conditions.

Figures 5 and 6 depict the journal eccentricity and attitude angle versus increasing specific pressure at rotational speeds of 4 and 12 krpm. The predictions are in good agreement with the tests data for specific pressures lower than 800 kPa (112 psi). Beyond this specific pressure, the predictions show a higher journal eccentricity perhaps due to thermo-elastic deformations not accounted for in the model. Ref. [15] does not list oil exit temperature rises that could be significant as the applied load and operating speed increase.

Figure 7 shows the direct stiffness K_{YY}, along the static load direction, increases nonlinearly with the applied load. K_{XX} is a fraction of K_{YY} and varies linearly with applied load. The predictions agree favorably with the measurements. Figure 8 depicts the cross-coupled stiffness coefficients with $K_{XY} < -K_{YX}$. Predictions from the model agree well with the negative stiffness coefficient, K_{XY}, whose magnitude is as large as the main direct K_{YY} coefficient.

Figures 9 and 10 depict the direct and cross-coupled damping coefficients versus specific pressure. Note that $C_{YY} > C_{XX}$ and $C_{XY} \sim C_{YX}$, as expected. The predictions agree very well with the test data at the high rotor speed (10 krpm). Note that the tests and model predictions show the bearing has more damping at the low journal speed. That is, damping coefficients are strong functions of the lubricant viscosity and journal eccentricity rather than rotational speed.

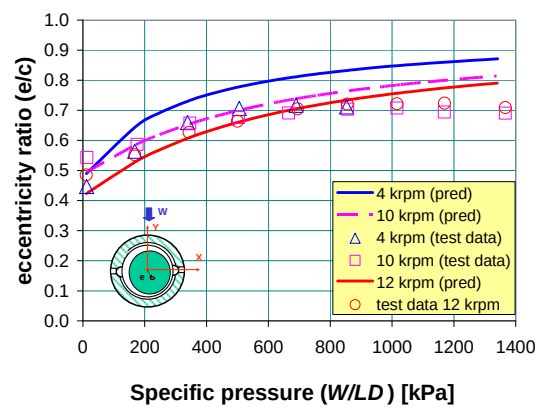

Fig. 5 Journal eccentricity vs. specific pressure for pressure dam bearing. Predictions and test data [15].

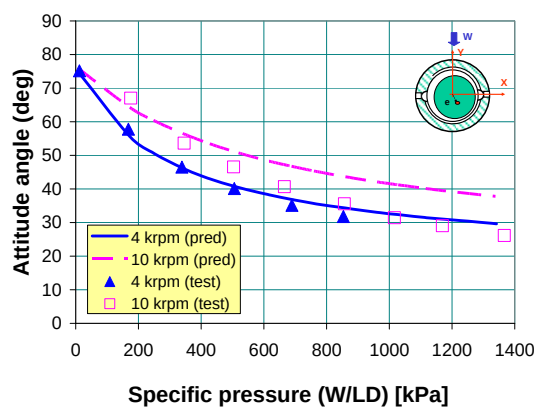

Fig. 6 Journal attitude angle vs. specific pressure for pressure dam bearing. Predictions and test data [15] at two rotor speeds

Copyright © 2012 by ASME

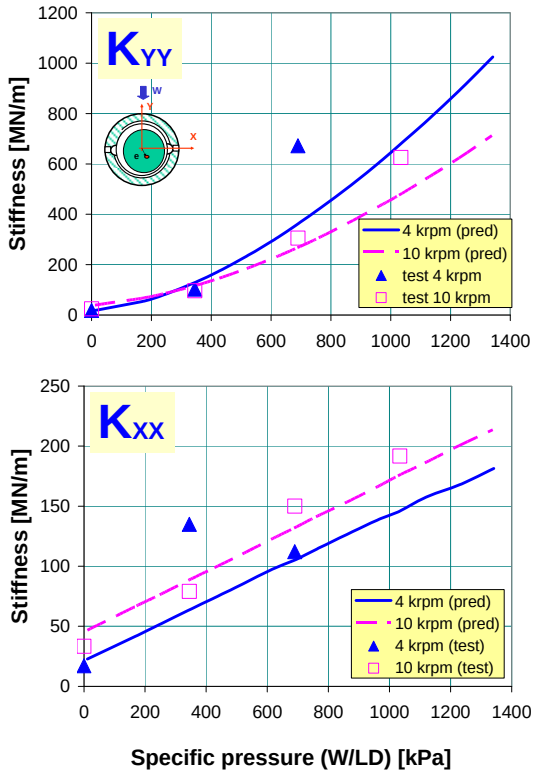

Fig. 7 Direct stiffnesses (K_{YY}, K_{XX}) vs. specific pressure for pressure dam bearing. Predictions and test data [15].

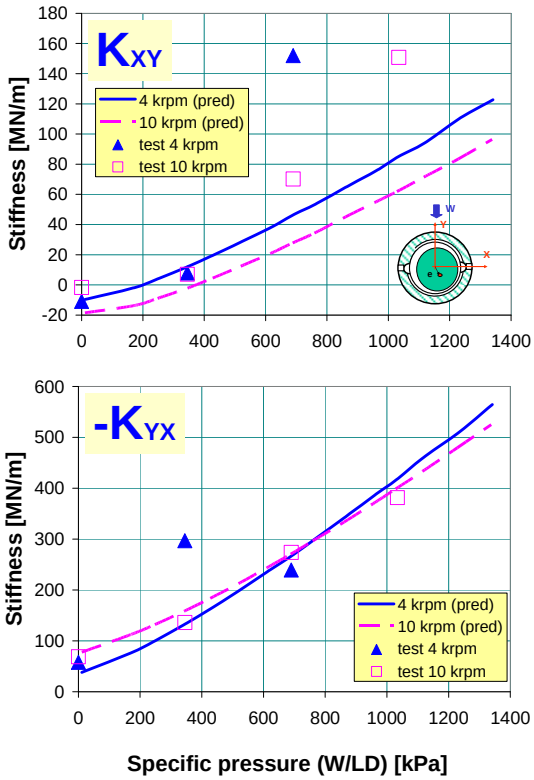

Fig. 8 Cross stiffnesses (K_{XY}, $-K_{YX}$) vs. specific pressure for pressure dam bearing. Predictions and test data [15].

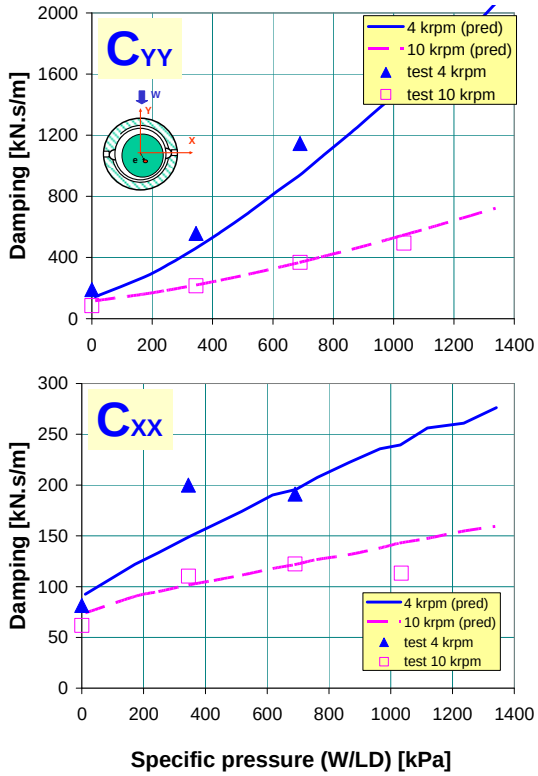

Fig. 9 Direct damping coeffs (C_{YY}, C_{XX}) vs. specific pressure for pressure dam bearing. Predictions and test data [15].

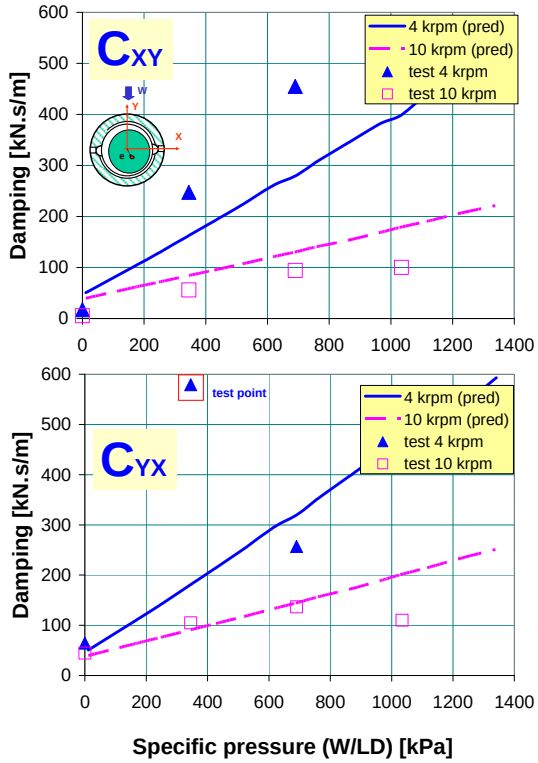

Fig. 10 Cross damping (C_{XY}, $-C_{YX}$) vs. specific pressure for pressure dam bearing. Predictions and test data [15].

Copyright © 2012 by ASME

Figure 11 shows the predicted inertia coefficients versus specific pressure for operation at 10 krpm. The predictions for other journal speeds are nearly identical and not shown for brevity. Table 2 lists the experimental force coefficients extracted from Ref. [15]. Note that the test values are much higher than the predictions and for the most part do not follow any trend[1]. The predictions, however, serve to evaluate the validity of the experimental force coefficients.

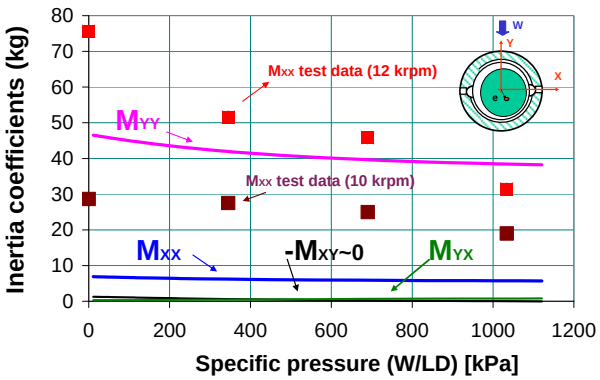

Fig. 11 Predicted fluid inertia coefficients vs. specific pressure for pressure dam bearing operating at 10 krpm. Test data [15] at two rotor speeds.

Note that for the studied thin film radial bearing and operating conditions, the squeeze film Reynolds number is rather small (Re_s~0.8); and hence conventional wisdom asserts that fluid inertia effects should be negligible. However, the prediction of inertia force coefficients demonstrates that the dynamic stiffnesses of the bearing (K-$\omega^2 M$) are largely affected by fluid inertia at high whirl frequencies (rotor speeds). Note that M_{YY}~45 kg is a rather large physical magnitude and, at 10 krpm (Ω=1048 rad/s), the product $\Omega^2 M_{YY}$ = 51 MN/m is a significant fraction of the static stiffness K_{YY}. To stress the paramount effect of fluid inertia, Figure 12 shows the ratio $\left[1-\Omega^2 \frac{M_{\alpha\beta}}{K_{\alpha\beta}}\right]$ versus specific pressure. Fluid inertia reduces significantly the dynamic stiffness, K_{YY} - $\omega^2 M_{YY}$, along the load direction. Note that this effect is more pronounced at the lowest load where the dynamic stiffness is just ~20% of the static stiffness. The reduction is remarkable!

To close the discussion, theory [3] predicts an inertia coefficient

$$M_{XX} = M_{YY} = \pi \rho \frac{L}{c}\left(\frac{D}{2}\right)^3 \left(1-\frac{\tanh\left(L/D\right)}{L/D}\right) = 35.1 \text{ kg} \qquad (22)$$

for a cylindrical journal bearing with uniform clearance c and for motions about the journal center (no load condition). The numerical predictions are larger since the test bearing has a relief groove and a pressure dam.

[1] The experimental uncertainty for the inertia coefficients could be as large as 30% of the reported value [15].

Table 2. Experimental fluid inertia coefficients in Ref. [15]

Speed rpm	Specific pressure kPa	M_{XX}	M_{XY} kg	M_{YX}	M_{YY}
4000	**0**	61.8	0.0	0.0	60.3
	345	0.0	0.0	-73.1	0.0
	690	0.0	0.0	0.0	0.0
6000	**0**	39.5	0.0	0.0	46.4
	345	34.4	0.0	0.0	0.0
	690	0.0	0.0	-44.2	0.0
8000	**0**	34.8	7.6	32.8	9.8
	345	30.1	0.0	0.0	24.2
	690	0.0	0.0	-33.3	0.0
	1034	0.0	0.0	-59.7	0.0
10000	**0**	28.6	9.1	21.0	18.5
	345	27.5	9.5	0.0	34.6
	690	25.0	0.0	0.0	0.0
	1034	19.0	0.0	0.0	0.0
12000	**0**	75.6	12.3	72.2	-7.6
	345	51.6	11.6	36.5	18.2
	690	45.8	11.5	0.0	0.0
	1034	31.4	0.0	67.1	0.0

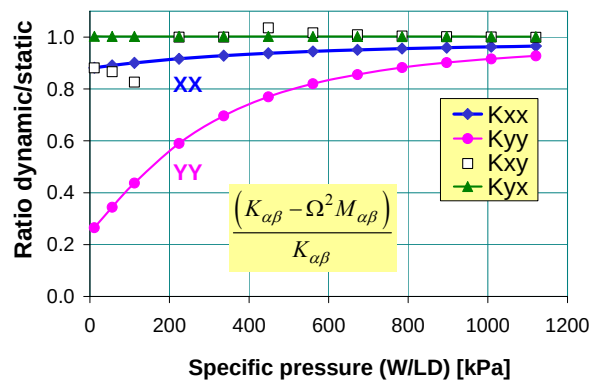

Fig. 12 Ratio of dynamic to static stiffnesses vs. specific pressure for a pressure dam bearing operating at 10 krpm. Predictions only.

CONCLUSIONS

Accurate prediction of the linearized force coefficients from radial fluid film bearings supporting rotating machinery is vital to predict and to validate the dynamic response and stability of a rotor-bearing system. To date most computational models represent the bearing dynamic reaction forces in terms of stiffness (**K**) and damping (**C**) force coefficients. However, modern machinery operates at ever increasing rotational speeds to increase power delivery. At high excitation frequencies[2], fluid inertia does affect the forced response of fluid film bearings by reducing their dynamic stiffness coefficients. Thus, modern predictive tools extend the linear force model to include fluid inertia coefficients (**M**).Thus, the dynamic force

[2] The most important frequency is synchronous with rotor speed (ω=Ω). Subsynchronous whirl frequencies coinciding with rotor-bearing system natural frequencies are relevant to the stability of a rotor-bearing system.

Copyright © 2012 by ASME

reaction vector from a fluid film bearing is $-\mathbf{F} = \mathbf{K}\,\mathbf{z} + \mathbf{C}\,\dot{\mathbf{z}} + \mathbf{M}\,\ddot{\mathbf{z}}$ with $\mathbf{z} = \{x, y\}^T$.

The paper details a physical analysis and finite element method (FEM) description to evaluate numerically bearing force coefficients (**K,C,M**). The procedure could be applied to an existing computational program to deliver bearing mass coefficients (**M**) with a minimum of extra computational cost and maximum expedience. The FEM can be applied to complicated bearing geometries representative of commercial applications.

Predictions from the model are benchmarked against experimental results for the static eccentricity and dynamic force coefficients obtained with a commercial size pressure dam bearing operating at moderate to high rotor speeds (12 krpm) and static loads as large as 12 kN. Representative test data is obtained from Ref. [15]. The correlations between predictions and measurements for static journal eccentricity and attitude angle, as well as for the direct stiffness and damping coefficients, are good albeit showing discrepancies as the applied static load on the bearing increases (max. W/LD = 1,345 kPa). The bearing operates under laminar flow conditions, the modified film Reynolds number ($\rho\Omega c^2/\mu$) < 1 at the highest rotor speed (12 krpm). Nonetheless, the test results and predictions show large magnitude added mass coefficients due to fluid inertia effects. These coefficients largely affect the dynamic stiffness of the bearing, in particular for operation with a low static load. Hence, igoring fluid inertia coefficients in a rotordynamic analysis could lead to predicted system natural frequencies that are higher than the actual values.

NOMENCLATURE

c	Nominal film (pad) clearance [m]
c_m	Bearing assembled clearance [m]
$C_{\sigma\beta}$	Bearing damping force coefficients; $_{\sigma,\,\beta = X,\,Y}$ $\left[\mathrm{N{\cdot}s/m}\right]$
D	Journal diameter [m]
e_X, e_Y	Journal center eccentric displacements [m]
F_X, F_Y	Fluid film bearing reaction forces [N]
h	Pad film thickness, $c - r_P\cos(\Theta-\Theta_P) + e_X\cos(\Theta) + e_Y\sin(\Theta)$ [m]
h_X, h_Y	$\cos(\Theta)$, $\sin(\Theta)$
$\boldsymbol{i}$	Imaginary unit ($\sqrt{-1}$)
$K_{\sigma\beta}$	Bearing stiffness coefficients; $_{\sigma,\,\beta = X,\,Y}$ $\left[\mathrm{N/m}\right]$
L	Journal bearing axial length [m]
$M_{\sigma\beta}$	Fluid inertia coefficients; $_{\sigma,\,\beta = X,\,Y}$ $\left[\mathrm{N/m}\right]$
n_{pe}	Number of nodes per finite element
N_{em}	Number of elements in flow domain
P	Film pressure [Pa]
P_a	Ambient pressure [Pa]
P_{cav}	Lubricant cavitation pressure [Pa]
P_S	Supply pressure [Pa]
P_0	Zeroth-order (equilibrium) pressure [Pa]
P_σ	First-order pressure fields; $_{\sigma,\,\beta = X,\,Y}$ [Pa/m]
q_η	Volumetric flow rate per unit length [m^2/s]
R	½ D. Journal radius, [m]
Re_s	$\left(\rho\omega h^2 / \mu\right)$. Squeeze film Reynolds number.
r_p	(c-c_m). Pad preload [m]
t	Time [s]
W_X, W_Y	Componentsof applied static load,
(x, y, z)	Coordinate system on plane of bearing (x= $R\Theta$)
(X, Y)	Inertial coordinate system
$Z_{\sigma\beta}$	Impedance force coefficients $\left(K_{\sigma\beta} - \omega^2 M_{\sigma\beta} + \mathbf{i}\omega C_{\sigma\beta}\right)$, $_{\sigma,\,\beta = X,\,Y}$ $\left[\mathrm{N/m}\right]$
Δe_X, Δe_Y	Dynamic displacements of journal center [m]
Θ	$\left(x/R\right)$. Circumferential coordinate [rad],
Θ_l, Θ_t, Θ_p	Arc pad leading and trailing edges, angle of min. film thickness (offset angle) [rad]
μ	Fluid viscosity [Pa-s]
Γ^e	Element boundary
ρ	Fluid density [kg/m^3]
ϕ	Journal attitude angle [°]
$\left\{\Psi_i\right\}_{=1}^{n_{pe}}$	Finite element shape functions
Ω	Rotor speed [rad/s]
ω	whirl frequency [rad/s]
Ω^e	Finite element sub-domain

Subscripts

S, a	Supply and ambient condition

Superscripts

e	element

Vectors and matrices

$\mathbf{k^e}$, $\mathbf{K_G}$	Fluidity matrices, element & global $\mathbf{K_G} = \mathbf{L_G}\,\mathbf{L_G^T}$
$\mathbf{q^e}$, $\mathbf{Q_G}$	Nodal flow rate vectors, element & global
$\mathbf{f^e}$, $\mathbf{F_G}$	Shear & squeeze flow rate vectors, element & global
$\bar{\mathbf{P}}_{\mathbf{0}}^{\mathbf{e}}$, $\bar{\mathbf{P}}_{\mathbf{G_0}}$	Nodal zeroth-order pressures, element & global
$\bar{\mathbf{P}}_{\boldsymbol{\sigma}}^{\mathbf{e}}$, $\bar{\mathbf{P}}_{\mathbf{G}_\sigma}$	Nodal first-order pressures, element & global σ=X,Y

ACKNOWLEDGMENTS

Thanks to Professor Dara Childs and his students for conducting exhaustive dynamic load measurements with a myriad of fluid film bearings and seals and identifying their rotordynamic force coefficients. The test results have not been always easily understood. This effort aims to close the bridge between theoretical predictions and measurements.

REFERENCES

[1] Boncompain, R., Fillon M., and Frene, J., 1986, "Analysis of Thermal Effects in Hydrodynamic Bearings," ASME J. Trib, **108**(2), pp. 219-224.

[2] Kucinschi, B., Fillon M., Pascovici, M., and Frene, J., 2000, "A Transient Thermoelastohydrodynamic Study of Steadily Loaded Plain Journal Bearings using Finite

Copyright © 2012 by ASME

Element Method Analysis," ASME J. Trib, **122**, pp. 219-226.

[3] Reinhart, F., and Lund, J. W., 1975, "The Influence of Fluid Inertia on the Dynamic Properties of Journal Bearings," ASME J. Lub. Tech., **97**, pp 154-167.

[4] Smith, D. L., 1975, "Journal Bearing Dynamic Characteristics-Effect of Inertia of Lubricant," Proc. IMechE., Paper No. 21, **179,** Part J: J. Engineering Tribology, pp 37-44.

[5] San Andrés, L., and Vance, J., 1987, "Effect of Fluid Inertia on Squeeze Film Damper Forces for Small Amplitude Circular Centered Motions," ASLE Trans., **30**, 1, pp. 69-76.

[6] San Andrés, L., 2009, "Thermal Analysis of Finite Length Journal Bearings Including Fluid Inertia," Modern Lubrication Theory," Notes 7, Texas A&M University, https://repository.tamu.edu/handle/1969.1/93197 , [accessed May 2010]

[9] Braun, M.J., and Hannon, W.M., 2010, "Cavitation Formation and Modelling for Fluid Film Bearings: a Review," Proc. IMechE, **224,** Part J: J. Engineering Tribology, pp. 839-863.

[10] Klit, P. and Lund, J. W., 1988, "Calculation of the Dynamic Coefficients of a Journal Bearing Using a Variational Approach," ASME J. Trib, **108**, pp. 421 - 425.

[11] Reddy J. N., Gartling, D. K., 2001, *The Finite Element Method in Heat transfer and Fluid Dynamics*, CRC Press, Florida, Chap. 2.

[12] San Andrés, L., and Delgado, A., 2012, "A Novel Bulk-Flow Model for Improved Predictions of Force Coefficients in Grooved Oil Seals Operating Eccentrically," ASME J. Eng. Gas Turbines Power, **134**, 022509.

[13] Ferron, J., Frene, J., and R. Boncompain, 1983, "A Study of the Thermohydrodynamic Performance of a Plain Journal Bearing Comparison between Theory and Experiments," ASME J. Trib., **105**, pp. 422-428,

[14] Brito, F.P., Miranda, A.S., Bouter, J., and Fillon, M., 2007, "Experimental investigation on the Influence of Supply temperature and Supply Pressure on the Performance of a Two-Axial Groove Hydrodynamic Journal Bearing," ASME J. Trib., **129**, pp. 98-105.

[15] Al-Jughaiman, B., and Childs, D., 2007, "Static and Dynamic Characteristics for a Pressure-Dam Bearing," ASME Paper No. GT2007-25577, Proc. ASME Turbo Expo 2007 Conference, May 14-17, Montreal, Canada.

[16] Nicholas, J., and Allaire, P., 1980, "Analysis of Step Journal Bearings-Finite Length and Stability," ASLE Trans., **22**, pp. 197-207.

Copyright © 2012 by ASME